The Cryosphere Discuss., 9, 5647–5680, 2015
www.the-cryosphere-discuss.net/9/5647/2015/
doi:10.5194/tcd-9-5647-2015

The Cryosphere Discussions
Open Access
EGU

Anomalously-dense firn in an ice-shelf channel revealed by wide-angle radar

R. Drews[1], J. Brown[2], K. Matsuoka[3], E. Witrant[4], M. Philippe[1], B. Hubbard[5], and F. Pattyn[1]

[1]Laboratoire de Glaciologie, Université Libre de Bruxelles, Brussels, Belgium
[2]Aesir Consulting LLC, Missoula, MT, USA
[3]Norwegian Polar Institute, Tromsø, Norway
[4]Université Grenoble Alpes/CNRS, Grenoble Image Parole Signal Automatique, 38041 Grenoble, France
[5]Aberystwyth University, Aberystwyth, Wales, UK

Received: 23 September 2015 – Accepted: 6 October 2015 – Published: 21 October 2015

Correspondence to: R. Drews (rdrews@ulb.ac.be)

Published by Copernicus Publications on behalf of the European Geosciences Union.

Abstract

The thickness of ice shelves, a basic parameter for mass balance estimates, is typically inferred using hydrostatic equilibrium for which knowledge of the depth-averaged density is essential. The densification from snow to ice depends on a number of local factors (e.g. temperature and surface mass balance) causing spatial and temporal variations in density–depth profiles. However, direct measurements of firn density are sparse, requiring substantial logistical effort. Here, we infer density from radio-wave propagation speed using ground-based wide-angle radar datasets (10 MHz) collected at five sites on Roi Baudouin Ice Shelf (RBIS), Dronning Maud Land, Antarctica. Using a novel algorithm including traveltime inversion and raytracing with a prescribed shape of the depth–density relationship, we show that the depth to internal reflectors, the local ice thickness and depth-averaged densities can reliably be reconstructed. For the particular case of an ice-shelf channel, where ice thickness and surface slope change substantially over a few kilometers, the radar data suggests that firn inside the channel is about 5 % denser than outside the channel. Although this density difference is at the detection limit of the radar, it is consistent with a similar density anomaly reconstructed from optical televiewing, which reveals 10 % denser firn inside compared to outside the channel. The denser firn in the ice-shelf channel should be accounted for when using the hydrostatic ice thickness for determining basal melt rates. The radar method presented here is robust and can easily be adapted to different radar frequencies and data-acquisition geometries.

1 Introduction

As a snow layer deposited at the ice-sheet surface is progressively buried by subsequent snowfall, it transforms to higher-density firn under the overburden pressure. The firn–ice transition, marked by the depth at which air bubbles are isolated, occurs at a density of approximately 830 kg m^{-3} at depths typically ranging from 30–120 m in po-

TCD
9, 5647–5680, 2015

lar regions (Cuffey and Paterson, 2010, chapter 2). Densification continues until air bubbles transform to clathrate hydrates and pure ice density is reached ($\rho_i \approx 917\,\mathrm{kg\,m^{-3}}$). The precise nature of this densification depends on a number of local factors that may also vary temporally (Arthern et al., 2010), including surface density and stratification (Hörhold et al., 2011) as well as surface mass balance and temperature (e.g. Herron and Langway, 1980). Recent studies also highlight the role of microstructure (Gregory et al., 2014) and impurities (Hörhold et al., 2012; Freitag et al., 2013a, b).

Knowledge of the depth–density profile and its spatial and temporal variability is important for a number of applications: (i) to determine the age difference of enclosed air bubbles and the surrounding ice in ice cores (Bender et al., 1997), (ii) to determine the depth and the cumulative mass above radar reflectors in order to map surface mass balance with radar (Waddington et al., 2007; Eisen et al., 2008), (iii) to interpret the seasonality of surface elevation changes (Zwally and Jun, 2002; Ligtenberg et al., 2014) in terms of surface mass balance, firn compaction, and dynamic thinning (e.g. Wouters et al., 2015); and (iv) to infer ice-shelf thickness for mass balance estimates (Rignot et al., 2013; Depoorter et al., 2013) from hydrostatic equilibrium (Griggs and Bamber, 2011).

Density profiles are most reliably retrieved from ice/firn cores either by measuring discrete samples gravimetrically, or by using continuous dielectric profiling (Wilhelms et al., 1998) or X-ray tomography (Kawamura, 1990; Freitag et al., 2013a). Techniques such as gamma-, neutron-, laser-, or optical-scattering (Hubbard et al., 2013 and references therein) circumnavigate the labour intensive retrieval of an ice core and only require a borehole which can rapidly be drilled using hot water.

All of the aforementioned techniques, however, remain point measurements requiring substantial logistics. A complementary way is to exploit the density dependence of radio-wave propagation speed. The principle underlying the technique involves illuminating a reflector with different ray paths such that both the reflector depth and the radio-wave propagation speed may be calculated using methods such as the Dix inversion (Dix, 1955), semblance analysis (e.g. Booth et al., 2010, 2011), interferometry

TCD
9, 5647–5680, 2015

(Arthern et al., 2013), or traveltime inversion based on raytracing (Zelt and Smith, 1992; Brown et al., 2012). A typical acquisition geometry is to position receiver and transmitter with variable offsets so that the sub-surface reflection point remains the same for horizontal reflectors (common-midpoint (CMP) surveys, e.g. Murray et al., 2000; Winebrenner et al., 2003; Hempel et al., 2000; Eisen et al., 2002; Bradford et al., 2009; Blindow et al., 2010). Alternatively, only the receiver can be moved (Fig. 1) resulting in what is sometimes referred to as wide-angle reflection and refraction (WARR, Hubbard and Glasser, 2005, p. 165) geometry. In all cases, density can be inferred from the radar-wave speed using density–permittivity relations (e.g. Looyenga, 1965; Wharton et al., 1980; Kovacs et al., 1995).

Here, we investigate six WARR measurements collected in December 2013 on Roi Baudouin Ice Shelf (RBIS), Dronning Maud Land, Antarctica. The WARR sites are part of a larger geophysical survey imaging an ice-shelf pinning-point and a number of ice-shelf channels which are about 2 km wide and can extend longitudinally from the grounding-line to the ice-shelf front (Le Brocq et al., 2013). Ice inside the channels is thinner, sometimes more than 50 % (Drews, 2015), and the surface is depressed causing the elongated lineations visible in satellite imagery (Fig. 2). Basal melting inside channels can be significantly larger (Stanton et al., 2013), correspondingly influencing ice-shelf stability (Gladish et al., 2012; Sergienko, 2013).

The basal mass balance inside the channels can be mapped from remote-sensing assuming mass conservation (e.g. Dutrieux et al., 2013). This approach calculates ice thickness from considerations of hydrostatic equilibrium which entails two pitfalls: (i) bridging stresses can prevent full relaxation to hydrostatic equilibrium (Drews, 2015), and (ii) it may not account for small-scale variations in material density. Evidence for small-scale changes in density was suggested by Langley et al. (2014) and Drews (2015), who found that the surface mass balance can be be locally elevated within the concave surface associated with the ice-shelf channels, which in turn may locally imprint the densification processes. Atmospheric models typically operate with a hor-

TCD
9, 5647–5680, 2015

izontal gridding coarser than 5 km (Lenaerts et al., 2014) and cannot resolve such small-scale variations in surface mass balance and density.

Herein, we calculate densities from WARR sites using traveltime inversion and raytracing (Sect. 2). The dataset is supplemented with densities based on optical televiewing (OPTV) of two boreholes (Fig. 2; Sect. 3). In Sects. 4 and 5, we compare both methods and discuss density anomalies associated with the ice-shelf channels. We present our conclusions about the derivation of density from radar in general, and the density anomalies in ice-shelf channels in particular in Sect. 6, and discuss consequences of our findings for estimating basal melt rates in ice-shelf channels.

2 Development of a new algorithm to infer density from wide-angle radar

We describe the propagation of the radar wave for each offset as a ray travelling from the transmitter via the reflection boundary to the receiver (Fig. 1). Using a coordinate system where x is parallel to the surface and z points vertically downwards, the raypaths are determined by the spatially variable radio-wave propagation speed $v(x,z)$ which is primarily determined by density; unless $v(x,z)$ is constant, raypaths are not straight but bend following Fermat's principle of minimizing the traveltime between transmitter and receiver. The geometry depicted in Fig. 1 is common in seismic investigations and multiple techniques exist for deriving the velocities from recorded traveltimes (Yilmaz, 1987).

Similar to what has been done for wide-angle radar measurements in Greenland (Brown et al., 2012), we follow a variation of the approach delineated by Zelt and Smith (1992). Brown et al. (2012) measured common midpoint returns with a 100 MHz radar. They used a raytracing forward model and inferred bulk densities of individual intervals (hereafter interval densities) by inverting reflector depths and interval velocities for single reflectors from top to bottom (a.k.a. layer stripping). In this paper, we use a 10 MHz radar providing improved depth penetration at the expense of lower spatial resolution. In order to prevent small errors in interval densities and velocities associ-

TCD
9, 5647–5680, 2015

ated with shallow reflectors from being handed downwards, we refine the method by parameterizing a monotonous depth–density function, and by inverting simultaneously for a set of parameters specifying the density and all reflector depths, described below.

2.1 Experimental setup

The radar consists of resistively loaded dipole antennas (10 MHz) linked to a 4 kV pulser (Kentech) for transmitting, and to a digitizing oscilloscope (National Instruments, USB-5133) for receiving (Matsuoka et al., 2012a). Figure 1 illustrates the acquisition geometry in which the transmitter remained at a fixed location and the receiver was moved incrementally farther away at 2 m intervals. The axis between transmitter and receiver at Sites 1, 2, 4, 5 and 6 were aligned across-flow (all antennas are parallel to the flow) because we expect the ice thickness to vary little in across-flow direction and therefore internal reflectors are less likely dipping. For the same reason Site 3, which is located inside an ice-shelf channel, was aligned parallel to the channel because in this particular area ice thickness varies mostly in across-flow direction. The transmitter–receiver distance was determined with measuring tape, and recording was triggered by the direct air wave. Processing of the radar data included horizontal alignment of the first arrivals (a.k.a. t_0 correction), dewow filtering, Ormsby bandpass filtering and the application of a depth-variable gain. Because triggering was done with the direct air-wave, a static time shift was added to each trace to account for the delayed arrival of the air wave for increasing offsets.

In multi-offset surveys, the traveltime of internal reflectors increases hyperbolically with increasing offset (e.g. Dix, 1955) while the surface wave (traveling in the firn column directly from transmitter to receiver) has a linear moveout. The maximum amplitude of the basal reflector was detected automatically and shifted with a constant offset to the first break. Internal reflectors were hand-picked. Figure 3 shows radargrams collected at all sites with the picked reflectors that were used for the analysis. The maximum offset for each site was chosen to equal approximately the local ice thickness. At Site 6, basal and internal reflectors are overlaid with signals from off-angle

TCD
9, 5647–5680, 2015

reflectors and cannot unambiguously be picked. We present the data here to exemplify a case for which WARR does not yield reliable results and exclude this site from further analysis.

2.2 Model parameterization and linearization

The traveltime t_{N_r,N_o} of a ray reflected from a reflector N_r ($r \in [1,R]$) at depth D_r measured at offset N_o ($o \in [1,O]$) is given by a line integral over the inverse of the velocity v along the raypath L (extending from the transmitter to the receiver via the reflection boundary).

$$t_{N_r,N_o} = \int_{L(\boldsymbol{m}_v,D_r)} \frac{1}{v(\boldsymbol{m}_v)} \mathrm{d}l \tag{1}$$

Figure 1 illustrates the notation. For each site, we pick a number of reflectors at different depths $\boldsymbol{m}_D = (D_1,\ldots,D_R)^T$, and we parameterize the velocity function as a function of density using the model parameters $\boldsymbol{m}_v$. We use an inverse method to reconstruct both the reflector depths and the velocity profile from the measured traveltimes.

The traveltime is a non-linear function of the model parameters (and hence the inversion results maybe non-unique) because L depends on both the initially unknown radio-wave propagation speed as well as the reflector depth. The velocity between two radar reflectors is often represented as piecewise constant or piecewise linear (Brown et al., 2012), making the model parameters $\boldsymbol{m}_v$ either the interval velocities or the interval velocity gradients, respectively. Here, we introduce additional constraints from Hubbard et al. (2013) who fit a depth profile of density of the form:

$$\rho = 910 - Ae^{-rz} \tag{2}$$

to density measurements of the borehole recovered at RBIS in 2010. The parameters A and r are tuning parameters for the surface density and the densification length,

TCD
9, 5647–5680, 2015

respectively. We relate density to the radio-wave propagation speed v using the CRIM equation (Wharton et al., 1980; Brown et al., 2012):

$$\rho = \frac{cv^{-1} - 1}{cv_{\mathrm{i}}^{-1} - 1}\rho_{\mathrm{i}}, \tag{3}$$

where $v_{\mathrm{i}} = 168\,\mathrm{m\,\mu s^{-1}}$ is the radio-wave propagation speed in pure ice and c is the speed of light in a vacuum.

Combining Eqs. (2) and (3) leads to:

$$v(A, r) = \frac{c}{C\rho(A, r) + 1} \tag{4}$$

with $C = \frac{1}{\rho_{\mathrm{i}}}(\frac{c}{v_{\mathrm{i}}} - 1)$ and $\boldsymbol{m}_{\mathrm{v}} = (A, r)^T$. We use Eq. (4) and assume (i) that radio-wave propagation speed v only depends on density (i.e. excluding ice anisotropy), (ii) that density is horizontally homogeneous over the maximum lateral offset of the receiver ($\leq 404\,\mathrm{m}$) but varies with depth so that v only varies with depth in that interval; and (iii) that within this interval, internal reflectors are horizontal. We aim to detect lateral variations of the velocity profiles on larger scales (i.e. between Sites 1–5) by finding optimal sets of parameters $\boldsymbol{m} = (\boldsymbol{m}_{\mathrm{D}}, \boldsymbol{m}_{\mathrm{v}}) = (A, r, D_1, \ldots, D_R)^T \in \mathbb{R}^{N_{\mathrm{m}}}$ describing the data at each site. The number of model parameters $N_{\mathrm{m}} = R + 2$ depends on the number of reflectors.

Using Eq. (4) and approximating the integral through a summation over N_z depth intervals, Eq. (1) reads:

$$t_{N_{\mathrm{r}},N_{\mathrm{o}}}(\boldsymbol{m}) \approx \frac{1}{c}\sum_{i=1}^{N_z} l_{z_i}(\boldsymbol{m})\,(C\rho(\boldsymbol{m}_{\mathrm{v}}) + 1)\,. \tag{5}$$

TCD
9, 5647–5680, 2015

The problem is linearized using an initial guess (marked with superscript 0) and a first order Taylor expansion:

$$t_{N_r,N_o}(\boldsymbol{m}) \approx t^0_{N_r,N_o} + \sum_{j=1}^{N_m} \frac{\partial t_{N_r,N_o}}{\partial m_j}\bigg|_{m_j^0} (m_j - m_j^0). \tag{6}$$

An equation of type (Eq. 6) holds for all O offsets of all R reflectors and can be summarized in matrix notation

$$\boldsymbol{\varepsilon} = \mathbf{S}\Delta\boldsymbol{m} \tag{7}$$

where we define $\boldsymbol{\varepsilon} = t_{\mathrm{mod}} - t_{\mathrm{obs}} \in \mathbb{R}^{N_p}$ as a vector composed of the residuals between the observed (t_{obs}) and the modelled (t_{mod}) travetimes. N_p is the total number of picked datapoints for all reflectors (not all reflectors can be picked to the maximum offset O), $\mathbf{S} \in \mathbb{R}^{N_p \times N_m}$ is a matrix containing all partial derivatives, and $\Delta\boldsymbol{m} \in \mathbb{R}^{N_m}$ is the model update vector. One synthesized reflector is composed of more than 50 independent measurements and at each site $R = 4$ reflector (including the basal reflector) were picked. There are therefore six model parameters ($N_m = 4 + 2$ for four reflector depths and 2 parameters A and r describing the depth–density function) and the number of measurements (N_p) is typically larger than 200, turning Eq. (7) in an overdetermined system of equations.

The derivatives of Eq. (6) with respect to A and r are:

$$\frac{\partial t_{N_r,N_o}}{\partial A} = -\frac{C}{c} \sum_{i=1}^{N_z} l_{z_i} e^{-r z_i} \tag{8}$$

$$\frac{\partial t_{N_r,N_o}}{\partial r} = \frac{AC}{c} \sum_{i=1}^{N_z} z_i l_{z_i} e^{-r z_i} \tag{9}$$

TCD
9, 5647–5680, 2015

and $\frac{\partial t_{N_r,N_o}}{\partial D_n}$ ($n \in [1,R]$) follows from geometric considerations (Zelt and Smith, 1992):

$$\frac{\partial t_{N_r,N_o}}{\partial D_n} = 2\frac{\cos\Theta_{N_r,N_o}}{v(D_n)}\delta_{nr} \tag{10}$$

where Θ_{D_n,N_o} is the incidence angle of ray N_o at the reflector boundary $N_r = n$ (Fig. 1b); $\delta_{nr} = 1$ for $r = n$ and 0 otherwise.

An optimal set of model parameters $\boldsymbol{m}$ is found as follows: (i) starting with an initial estimate for the reflector depths $\boldsymbol{m}_D^0$ and the velocity model $\boldsymbol{m}_v^0$, a raytracing forward model (Sect. 2.3) calculates the expected traveltimes $t^0_{N_r,N_o}$ for a given set of transmitter–receiver offsets; the difference between modelled and observed traveltimes results in the misfit vector $\boldsymbol{\varepsilon}$ in Eq. (7), (ii) the overdetermined system is inverted for the unknown parameter-correction vector $\Delta\boldsymbol{m}$ (Sect. 2.4), and (iii) the parameter set is updated with $\boldsymbol{m}^1 = \boldsymbol{m}^0 + \Delta\boldsymbol{m}$ and serves as new input for the forward model. These steps are repeated iteratively until the parameter updates are negligible.

2.3 Raytracing forward model

We apply the raytracing model provided by Margrave (2011) to only reflected (and not refracted) rays. For a given set of reflectors in a $v(z)$ medium, no analytical solution exists which directly provides a raypath from the transmitter to a given offset via a reflection boundary. The problem is solved iteratively by calculating fans of rays with varying take-off angles until one ray endpoint emerges within a given minimum distance (≤ 0.5 m) to the receiver. For some $v(z)$ configurations no such ray can be found, indicating that the prescribed $v(z)$-medium does not adequately reproduce the observations.

TCD
9, 5647–5680, 2015

2.4 Inversion

To solve the inverse problem we seek the set of parameters $\boldsymbol{m}$ that minimizes the objection function J

$$J = \frac{1}{2}\boldsymbol{\varepsilon}^T \mathbf{C}_\mathrm{t}\boldsymbol{\varepsilon} + \frac{1}{2}\lambda(\boldsymbol{m}-\boldsymbol{m}_0)^T \mathbf{C}_\mathrm{M}(\boldsymbol{m}-\boldsymbol{m}_0) \tag{11}$$

in which the first term is the ℓ^2 norm of the traveltime residual vector weighted with $\mathbf{C}_\mathrm{t} = \mathrm{diag}\{\sigma_i^2\}$ where σ_i is the uncertainty of the traveltime picks. The second term is a regularization (weighted with $\mathbf{C}_\mathrm{m} = \mathrm{diag}\{\sigma_j^2\}$ where σ_j is the estimated uncertainty of the model parameters) penalizing solutions which are far from the initial guess. Regularization with the Lagrange multiplier λ is needed because outliers in the data are weighted disproportionally in a least-squares sense which can lead to overfitting the data.

We minimize J by updating $\boldsymbol{m}$ iteratively according to the Gauss–Newton method:

$$\boldsymbol{m}^{i+1} = \boldsymbol{m}^i - (\mathbf{S}^T\mathbf{C}_\mathrm{t}^{-1}\mathbf{S} + \lambda\mathbf{C}_\mathrm{m}^{-1})^{-1}\nabla J \tag{12}$$

with $\nabla J = \mathbf{C}_\mathrm{t}^{-1}\mathbf{S}\boldsymbol{\varepsilon} + \lambda\mathbf{C}_\mathrm{m}^{-1}(\boldsymbol{m}-\boldsymbol{m}_0)$. High values of λ result in a final model vector remaining close to the initial guess; lower values of λ allow for larger changes in the parameter updates. We stop iterating when changes in J are below an arbitrarily small threshold.

2.5 Sensitivity of the firn-air content

In order to compare different measurements at different locations, we decompose the ice shelf into two layers of ice (H_i) and air (H_A) so that $\overline{\rho}H = \rho_\mathrm{i}H_\mathrm{i} + \rho_\mathrm{a}H_\mathrm{A}$ and $H_\mathrm{i} + H_\mathrm{a} = H$ (i.e. $H_\mathrm{A} = \frac{\overline{\rho}-\rho_\mathrm{i}}{\rho_\mathrm{a}-\rho_\mathrm{i}}H$). The firn-air content H_A (with air density ρ_a) is a quantity independent of the local ice thickness (as long as the depth-averaged wave speed is determined below the fin-ice transition) and changes thereof indicate changes in the depth-averaged density due to a changing firn-layer thickness. The firn air content in

TCD
9, 5647–5680, 2015

Antarctica can vary from $H_A = 0$ m in blue ice areas up to $H_A = 45$ m for cold firn on the Antarctic plateau (Ligtenberg et al., 2014). Using the CRIM equation to determine H_A results in:

$$H_A = \frac{cH\rho_i(\frac{1}{\overline{v}} - \frac{1}{v_i})}{(\rho_a - \rho_i)(\frac{c}{v_i} - 1)}. \quad (13)$$

We consider errors in H_A from uncertainties in the depth-averaged radio-wave propagation speed ($\overline{v}$), and uncertainties in ice thickness (H):

$$\delta H_A^2 \approx \left(\frac{c\rho_i}{v^2(\rho_a - \rho_i)(\frac{c}{v_i} - 1)} H\delta\overline{v}\right)^2 + \left(\frac{c\rho_i(\frac{1}{\overline{v}} - \frac{1}{v_i})}{(\rho_a - \rho_i)(\frac{c}{v_i} - 1)}\delta H\right)^2. \quad (14)$$

Assuming $\delta\overline{v} \approx 1\,\%$, and $\delta H \approx 10\,\%$ renders the first term of Eq. (14) about eight times larger than the second for the parameter ranges considered here, and we therefore neglect errors in ice thickness for the error propagation. Equation (14) shows that the uncertainty of H_A scales with the local ice thickness so that small errors in the depth-averaged velocities ($< 1\,\%$) result in significant errors in terms of H_A. We use H_A as a sensitive metric for both comparing sites laterally and for illustrating uncertainties of the radar method. In the following, we use synthetic data to choose optimal parameters for the inversion, and to investigate how errors in the data propagate into the final depth–density estimates.

2.6 Testing with synthetic examples

To test the inverstion algortihm we use raytracing with a prescribed depth–density function and recording geometry ($A = 460\,\mathrm{kg\,m^{-3}}$, $r = 0.033\,\mathrm{m^{-1}}$; transmitter–receiver offsets between 30–300 m with 2 m spacing) to create a synthetic traveltime dataset with multiple reflectors. We first investigate if the solution is well constrained for ideal cases, and then we discuss effects of systematic and random errors in the data.

TCD
9, 5647–5680, 2015

We consider two ideal cases: a single reflector at 400 m depth, and two reflectors at 30 and 400 m depth. Using the forward model, we simulated a new set of reflectors with model parameters covering depth ranges of ±5 m from the ideal depths and depth–density functions defined by $r = 0.01$–$0.1\,\mathrm{m}^{-1}$ (A was fixed). This range in densities corresponds to firn-air contents from $H_A = 5$ to 50 m. The root-mean-square differences (Δt_{rms}) between the perturbed and the ideal reflector are equivalent to the first term of the objective function J (Eq. 11) and indicate how well constrained the solution is. Figure 4a illustrates that for a single reflector the solution is not well constrained, meaning that different sets of model parameters give similar results to the ideal solution (i.e. dense firn/shallower reflector or less-dense firn/deeper reflector). For example, positioning the reflector at 392 m depth with $r = 0.063\,\mathrm{m}^{-1}$ results in a firn-air content of about 11 m, whereas positioning the reflector at 410 m depth with $r = 0.014\,\mathrm{m}^{-1}$ corresponds to a firn-air content of approximately 40 m. Both cases have a small model-data discrepancy and are barely distinguishable from the ideal solution. Using two reflectors simultaneously better constrains the solution, particularly if the shallower reflector is above the firn–ice transition (Fig. 4b). We conclude from these simple test cases that using the basal reflector only is not enough. Multiple reflectors should be considered and inverted for simultaneously. Using this type of testing, we also find (i) that treating A as a free parameter introduces significant tradeoffs with r even for small noise levels. We therefore keep A fixed and assume in the following that the surface density is laterally uniform, (ii) plotting both terms of the objective function J (Eq. 11) vs. each other for different λ (a.k.a. L-Curve) helps to choose an optimal λ. We find that $\lambda \approx 0.1$ marks approximately the kink point between a too large model-data discrepancy on the one hand and overfitting on the otherhand. We keep $\lambda = 0.1$ from hereon to prevent overfitting, but note that results are largely independent of λ for $\lambda \ll 0.1$.

Next, we consider effects of random and systematic errors and simulate four ideal reflectors ($D_1 = 100$ m, $D_2 = 150$ m, $D_4 = 200$ m, $D_4 = 400$ m) to which we add normally distributed noise (i.e. simulating picking errors and variability in aligning the direct waves used for triggering) and linear trends (i.e. simulating accumulated errors in po-

TCD
9, 5647–5680, 2015

sitioning, unaccounted reflector dipping, etc.). We then tested the robustness of the inversion for different initial guesses, and different magnitudes of noise and systematic errors. We find that the limiting factor for the initial depth guess is the forward model which does not find raypaths for all offsets if the initial guess deviates more than about 15 m from the true solution. For all initial guesses deviating less than that, the inversion robustly recovers the true depths within decimeters even for noise levels with a mean amplitude of 5 times the sampling interval (0.01 µs). However, the inversion is most sensitive to trends in the data. For example, if reflectors systematically deviate from 0.04 to −0.04 µs for large offsets, reflector depths are reconstructed with an error of 2–3 m. The corresponding densities deviate in terms of firn-air content more than 5 m from the ideal solutions. We conclude from these test cases that reflectors need to be picked accurately (i.e. keeping the same phase within the individual wavelets); if systematic differences between forward model and data occur (e.g. the modeled reflector is tilted with respect to the observations) results should be interpreted with care.

2.7 Inversion of field data

For each site, three internal reflectors were handpicked (D_1–D_3) to complement the automatically detected basal reflector (D_4, Fig. 3). Initial guesses for reflector depths are based on standard linear regression in the traveltime^2–offset^2 diagrams (Dix, 1955); $r^0 = 0.033\,\mathrm{m}^{-1}$ and $A = 460\,\mathrm{kg\,m}^{-3}$ stem from the 2010 OPTV density profile (Hubbard et al., 2013).

We first checked the consistency of the picked internal reflectors and inverted for r and the depths of one internal reflector together with the basal reflector. The remaining two internal reflectors were not used for the inversion, but to validate the results. We did this for all three combinations (D_1–D_4, D_2–D_4, D_3–D_4) in order to check if internal reflectors have been picked with the correct phase. Results were considered consistent if the model-data discrepancy for each reflector was within ±0.02 µs (cf. radar sampling interval is 0.01 µs). Picking a wrong phase typically causes inconsistent results for one of the combinations. In such a case the corresponding reflector was re-picked.

TCD
9, 5647–5680, 2015

In a second step, we inverted for all five remaining reflector combinations containing three and four reflectors. We also considered a range for r^0 between 0.021 and 0.056 m^{-1} corresponding to a firn-air content of 24 and 9 m, respectively. Figure 5 illustrates an example where three reflectors were used for the inversion and one was left for validation: The model-data discrepancy is large for the initial guess. After the inversion, the model-data discrepancy is smaller for all reflectors including the reflector that was used for control only.

In general, the final results are more sensitive to the respective reflector combination than to the initial guess of r^0. For the latter we chose the one resulting in the smallest model data discrepancy ($r^0 = 0.033\,m^{-1}$). Differences between the final five parameter sets give a lower boundary for an error estimate.

3 Density from optical televiewing

Densities were evaluated independently from OPTV logs of two boreholes drilled in 2010 and 2014 (Fig. 2). OPTV exploits the density-dependence of backscattered light within the borehole. By lowering an OPTV device into boreholes, luminosity (i.e. density) profiles can be collected with a vertical resolution of millimeters (Hubbard et al., 2008). This has been demonstrated for the 2010 borehole at RBIS (Hubbard et al., 2013) and we refer to this reference for further details on the method. For the 2014 borehole we used the same relationship between luminosity and density as for the 2010 borehole. In both cases ice cores were also retrieved, and the luminosity–density curve for depths > 10 m has been validated with gravimetrically measured samples.

4 Results

Figure 6 and Table 1 summarize the derived depth–density functions, ice thicknesses, radio-wave propagation speeds, depth-averaged densities and the firn-air contents of the five WARR sites. The reconstructed thicknesses vary between 157–396 m (86 %

TCD
9, 5647–5680, 2015

percentage difference), the depth-averaged densities vary between 828–874 kg m^{-3} (~ 5 % percentage difference) and corresponding firn-air contents vary from 13.2–19.3 m (38 % percentage difference). For the five different reflector combinations at each site, the inverted ice thicknesses differ by less than 1.5 m (< 1 % percentage difference), the inverted depth-averaged densities differ by less than 10 kg m^{-3} (< 1 % percentage difference) and the final firn air contents differ by less than 3 m (< 17 % percentage difference; Fig. 6b–d). This indicates that the results are numerically robust to the combination of reflectors used, and that the local ice thickness and depth-averaged density can be determined with high-confidence. However, we cannot derive rigorous error estimates from the inversion itself. We found that picking the internal reflectors is the most sensitive step and, similar to Brown et al. (2012), we estimate that the depth-averaged velocity can be determined within ±1 %. We used this value to calculate errors for the depth-averaged densities and the equivalent firn-air content. These errors roughly take into account the assumptions of non-dipping reflectors, ice isotropy, and uncertainties of the density–permittivity model.

The estimated 1 % error on the (depth-averaged) radio-wave propagation speed translates into large error bars for the corresponding firn-air contents (Fig. 6d) impeding the comparison between sites. Nevertheless, Sites 2 and Sites 3 show lower firn-air contents (~ 13 m) than the other sites (~ 17 m).

To assess the derived depth–density profiles with an independent dataset, we compare Site 1 and Site 3 with the OPTV densities from the 2010 and 2014 boreholes, respectively (Fig. 7). Site 3 is located inside an ice-shelf channel, about 10 km north of the 2014 borehole located in the same channel. Site 1 is about 6 km south of the 2010 borehole (Fig. 2). Both radar WARR measurements and the OPTV logs show a depth–density profile which is denser inside than outside the ice-shelf channel. This increases our confidence that the WARR method developed here indeed picks up significant differences in firn-air content on small spatial scales.

TCD
9, 5647–5680, 2015

5 Discussion

5.1 Benefits of traveltime inversion using raytracing

A difference between the new study presented here and previous ones (e.g. Brown et al., 2012) is how the radio-wave propagation speed is parameterized. Previous studies used piece-wise linear or uniform speed between individual reflectors, while we parameterize the speed as a continuous function of depth (Eq. 4). Here, we examine the benefit of this approach for interpreting the radar results

A common problem when using the Dix inversion or semblance analysis is that the applied normal moveout (NMO) approximation presupposes small reflection angles (to linearize trigonometric functions) and small velocity contrasts (Dix, 1955). In our case reflection angles can be large ($< 45^{\circ}$), particularly near the maximum offsets; contrary to NMO, raytracing is not adversely influenced by wide incidence angles. NMO presupposes small velocity contrasts, because raypaths are approximated as oblique lines neglecting raybending from a gradually changing background medium. Traveltime inversion with raytracing equally relies on this approximation as long as interval velocities are assumed. In this study, we prescribe a realistic shape of a depth–density/velocity function which changes gradually with depth and raybending is adequately taken into account during the raytracing. We have tested both the small angle and the small velocity contrast limitations quantitatively by using the OPTV based depth–density/velocity function and raytracing in order to simulate synthetic traveltimes of reflectors at various depths (50–500 m) and horizontal offsets (50–500 m). We then used the synthetic traveltimes for calculating the reflector depths and the depth-averaged velocities (averaged from the surface to the reflector depths) subject to the NMO equations. Differences in depth-averaged velocities were smaller than 0.5 %, and differences in reflector depths were smaller than 0.5 m. Similar to the findings of Barrett et al. (2007), this confirms that in our case the NMO approximation essentially holds, even for comparatively large horizontal offsets and a continuously changing depth–velocity function. This must not always be the case and raytracing easily allows the NMO approximation to be checked

TCD
9, 5647–5680, 2015

for each specific setting. For the examples considered here, solutions based on the Dix inversion using the basal reflector only typically result in thicker ice and higher depth-averaged densities (and correspondingly lower firn-air contents, Fig. 6c and d).

Data collection in a WARR survey is faster than a common-midpoint survey because only the receiver (or transmitter) needs to be repositioned. A common-midpoint survey, on the other hand, more easily facilitates the corrections for dipping reflectors using dip-moveout (Yilmaz, 1987). The choice for the acquisition geometry thus depends on the time available in the field and on the glaciological setting (i.e. are dipping reflectors to be expected). Traveltime inversion can cope with both types of acquisition geometries.

The main advantages of the method applied here are primarily linked to a more robust inversion which is less sensitive to reflector delineation because reflectors are inverted simultaneously to constrain the density profile. First, prescribing a global depth–density/velocity function for all internal reflectors allows the coherency of the reflector picking to be checked by investigating different subsets of reflector combination to single out reflectors which were picked with the wrong phase (Sect. 2.7). This step is important, particularly when using lower frequencies as was the case here (10 MHz). At this stage the basal reflectors is useful, because it can be unambiguously identified. Once more than two shallow internal reflectors are reliably picked, we found that the inversion results were largely independent of the in- or exclusion of the basal reflector. Second, by inverting for reflectors simultaneously, it is less likely that deeper reflectors inherit uncertainties from shallower reflectors. This can happen when solving for reflectors individually where tradeoffs between interval velocities and the reflector depths are subsequently handed downwards. Third, when using interval velocities, the parameter set describing the depth-density/velocity function is larger than is the case here. For example, for four reflectors eight parameters are required when using interval velocities (four velocities and reflector depths, respectively), and only five parameters for the method applied here (r and four reflector depths). Simpler models with fewer model parameters are preferable when using inversion.

TCD
9, 5647–5680, 2015

The WARR data presented here were collected with a 10 MHz radar. The disadvantage of this low frequency is that fewer reflectors above the firn–ice transition can be picked at a lower resolution, relative to higher-frequency datasets (cf. Eisen et al. (2002) who derived an 8 % velocity error with a 25 MHz radar vs. a 2 % error with 200 MHz radar). We found that the method applied here can cope with the picking uncertainties at 10 MHz, whereas using Dix inversion frequently resulted in interval densities much larger than the pure ice density. The advantage of using a 10 MHz radar is that the entire ice column is illuminated, including the unambiguous basal reflector. This opens up the possibility for more sophisticated radar-wave velocity models including ice anisotropy originating from aligned crystal orientation fabric below the firn–ice transition (Drews et al., 2012; Matsuoka et al., 2012b). The radar dataset is also suited for other glaciological applications, for example: using the basal reflections for deriving ice temperature (via radar attenuation rates) from an amplitude vs. offset analysis (Winebrenner et al., 2003) and to constrain the alignment of ice crystals using multistatic radar as a large-scale Rigsby stage (Matsuoka et al., 2009).

5.2 Radar- and OPTV-inferred densities

We found velocity models for each site which adequately fit all reflector combinations. There is no systematic deviation larger than the picking uncertainty and hence there is no evidence that reflectors are dipping within the interval between minimum and maximum offset (≤ 404 m). The results are numerically robust for different reflector combinations, indicating equal validity for all results based on three reflectors or more (Sect. 2.7).

The derived depth–density functions cluster in two groups: Sites 1, 4, and 5 have a mean firn air-content of ~ 17 m whereas Sites 2 and 3 have lower values of ~ 13 m. While these differences are minor from a radar point-of-view, they are quite significant from an atmospheric-modeling point of view. For example, van den Broeke et al. (2008) propose that the firn-air content around the entire Antarctic grounding-line is bound between 13 (for the Dronning Maud Land area) and 19 m (for ice shelves in

TCD
9, 5647–5680, 2015

West Antarctica). Including transient effects, such as surface melt, the variability increases but typically stays within 5–20 m (Ligtenberg et al., 2014). Because the aforementioned models run on 27 km grids (approximately the size of our research area) they may overlook effects acting on smaller scales. However, with the estimated uncertainty of the depth-averaged wave speed (±1 %) the radar-derived variability in firn-air content is barely significant (Fig. 6d). Notwithstanding, we find that Site 1 (which is closest to the 2010 borehole) agrees closely with the OPTV of 2010, and a similarly good fit is found between Site 3 and the 2014 OPTV (both located inside the same ice-shelf channel, Fig. 7). The implications are two-fold: First, the correspondence between the OPTV-derived density variations and those derived from the WARR method provide independent validation of the latter technique. Second, the fact that both techniques show increased density within the surface channel indicates that the effect is real and should be accounted for by investigations based on hydrostatic equilibrium. Even though uncertainties remain (for example, we have no explanation for the similarly low firn-air content at Site 2) this shows that traveltime inversion and raytracing with a prescribed shape for the depth–density function can produce results which compare closely with densities derived from OPTV (exluding small-scale variability due to melt layers). It is yet unclear which mechanism causes the denser ice in ice-shelf channels, and further investigation is required for more general conclusions about density anomalies in ice-shelf channels. Regardless of the specific mechanism, the data presented here clearly show that this point requires attention, particularly when using mass conservation to derive basal melt rates in ice-shelf channels: errors in the firn-air content propagate approximately with a factor of ten into the hydrostatic ice thickness, which then substantially alters the magnitude of derived basal melt rates.

6 Conclusions

We have collected six WARR radar measurements on RBIS and used traveltime inversion in conjunction with raytracing to infer the local depth–density profiles. In the inver-

TCD
9, 5647–5680, 2015

sion, we prescribed a physically motivated shape for the depth–density function, which adequately takes curved raypaths and large reflection angles into account and easily allows to invert for multiple reflectors simultaneously. We find that this method produces robust results even with a comparatively low-frequency (10 MHz) radar system with correspondingly reduced spatial resolution and small numbers of internal reflectors used to constrain the density model. The inversion method is flexible and can easily be adapted to other acquisition geometries and radar frequencies. Ice thickness and depth-averaged densities/wave-speed are reconstructed within a few percent. Larger errors in the corresponding firn-air contents, however, impede detailed comparison between sites. Nevertheless, spatial variations in densities derived from both WARR radar and borehole OPTV show that the depth-density profile within a 2 km wide ice-shelf channel is denser inside than outside that channel. This density anomaly needs to be accounted for when using hydrostatic equilibrium to infer ice thickness, and has implications for using mass budgets methods to determine basal melting in ice-shelf channels. More data is needed to evaluate whether the density-anomaly observed here is a generic feature of ice-shelf channels in Antarctica.

Acknowledgements. This paper forms a contribution to the Belgian Research Programme on the Antarctic (Belgian Federal Science Policy Office), Project SD/SA/06A Constraining ice mass changes in Antarctica (IceCon) as well as the FNRS-FRFC (Fonds de la Recherche Scientifique) project IDyRA. We thank the InBev Baillet Latour Antarctica Fellowship for financing the RBIS fieldwork and the International Polar Foundation for providing all required logistics in the field. We thank in particular A. Hubert, K. Moerman, K. Soete, and L. Favier for support in the field. M. Philippe is partially funded through a grant from the “Fonds David et Alice Van Buuren”.

References

Arthern, R. J., Vaughan, D. G., Rankin, A. M., Mulvaney, R., and Thomas, E. R.: In situ measurements of Antarctic snow compaction compared with predictions of models, J. Geophys. Res., 115, F03011+, doi:10.1029/2009jf001306, 2010. 5649

TCD
9, 5647–5680, 2015

Arthern, R. J., Corr, H. F. J., Gillet-Chaulet, F., Hawley, R. L., and Morris, E. M.: Inversion for the density-depth profile of polar firn using a stepped-frequency radar, J. Geophys. Res.-Earth, 118, 1257–1263, doi:10.1002/jgrf.20089, 2013. 5650

Barrett, E. B., Murray, T., and Clark, R.: Errors in radar CMP velocity estimates due to survey geometry, and their implication for ice water content estimation, J. Environ. Eng. Geoph., 12, 101–111, doi:10.2113/JEEG12.1.101, 2007. 5663

Bender, M., Sowers, T., and Brook, E.: Gases in ice cores, P. Natl. Acad. Sci. USA, 94, 8343–8349, doi:10.1073/pnas.94.16.8343, 1997. 5649

Blindow, N., Suckro, S. K., Rückamp, M., Braun, M., Schindler, M., Breuer, B., Saurer, H., Simões, J. C., and Lange, M. A.: Geometry and thermal regime of the King George Island ice cap, Antarctica, from GPR and GPS, Ann. Glaciol., 51, 103–109, doi:10.3189/172756410791392691, 2010. 5650

Booth, A., Clark, R., and Murray, T.: Semblance response to a ground-penetrating radar wavelet and resulting errors in velocity analysis, Near Surf. Geophys., 8, 235–246, doi:10.3997/1873-0604.2011019, 2010. 5649

Booth, A., Clark, R., and Murray, T.: Influences on the resolution of GPR velocity analyses and a Monte Carlo simulation for establishing velocity precision, Near Surf. Geophys., 9, 399–411, doi:10.3997/1873-0604.2011019, 2011. 5649

Bradford, J. H., Harper, J. T., and Brown, J.: Complex dielectric permittivity measurements from ground-penetrating radar data to estimate snow liquid water content in the pendular regime, Water Resour. Res., 45, W08403, doi:10.1029/2008WR007341, 2009. 5650

Brown, J., Bradford, J., Harper, J., Pfeffer, W. T., Humphrey, N., and Mosley-Thompson, E.: Georadar-derived estimates of firn density in the percolation zone, western Greenland ice sheet, J. Geophys. Res.-Earth, 117, F01011, doi:10.1029/2011JF002089, 2012. 5650, 5651, 5653, 5654, 5662, 5663

Cuffey, K. and Paterson, W.: The Physics of Glaciers, 4th Edn., Academic Press, Burlington, MA, 2010. 5649

Depoorter, M. A., Bamber, J. L., Griggs, J. A., Lenaerts, J. T. M., Ligtenberg, S. R. M., van den Broeke, M. R., and Moholdt, G.: Calving fluxes and basal melt rates of Antarctic ice shelves, Nature, 502, 89–92, doi:10.1038/nature12567, 2013. 5649

Dix, C. H.: Seismic velocities from surface measurements, Geophysics, 20, 68–86, doi:10.1190/1.1438126, 1955. 5649, 5652, 5660, 5663, 5679

TCD
9, 5647–5680, 2015

Drews, R.: Evolution of ice-shelf channels in Antarctic ice shelves, The Cryosphere, 9, 1169–1181, doi:10.5194/tc-9-1169-2015, 2015. 5650

Drews, R., Eisen, O., Steinhage, D., Weikusat, I., Kipfstuhl, S., and Wilhelms, F.: Potential mechanisms for anisotropy in ice-penetrating radar data, J. Glaciol., 58, 613–624, doi:10.3189/2012JoG11J114, 2012. 5665

Dutrieux, P., Vaughan, D. G., Corr, H. F. J., Jenkins, A., Holland, P. R., Joughin, I., and Fleming, A. H.: Pine Island glacier ice shelf melt distributed at kilometre scales, The Cryosphere, 7, 1543–1555, doi:10.5194/tc-7-1543-2013, 2013. 5650

Eisen, O., Nixdorf, U., Wilhelms, F., and Miller, H.: Electromagnetic wave speed in polar ice: validation of the common-midpoint technique with high-resolution dielectric-profiling and -density measurements, Ann. Glaciol., 34, 150–156, doi:10.3189/172756402781817509, 2002. 5650, 5665

Eisen, O., Frezzotti, M., Genthon, C., Isaksson, E., Magand, O., van den Broeke, M. R., Dixon, D. A., Ekaykin, A., Holmlund, P., Kameda, T., Karlöf, L., Kaspari, S., Lipenkov, V. Y., Oerter, H., Takahashi, S., and Vaughan, D. G.: Ground-based measurements of spatial and temporal variability of snow accumulation in East Antarctica, Rev. Geophys., 46, RG2001, doi:10.1029/2006RG000218, 2008. 5649

Freitag, J., Kipfstuhl, S., and Laepple, T.: Core-scale radioscopic imaging: a new method reveals density–calcium link in Antarctic firn, J. Glaciol., 59, 1009–1014, doi:10.3189/2013JoG13J028, 2013a. 5649

Freitag, J., Kipfstuhl, S., Laepple, T., and Wilhelms, F.: Impurity-controlled densification: a new model for stratified polar firn, J. Glaciol., 59, 1163–1169, doi:10.3189/2013JoG13J042, 2013b. 5649

Gladish, C. V., Holland, D. M., Holland, P. R., and Price, S. F.: Ice-shelf basal channels in a coupled ice/ocean model, J. Glaciol., 58, 1227–1244, doi:10.3189/2012JoG12J003, 2012. 5650

Gregory, S. A., Albert, M. R., and Baker, I.: Impact of physical properties and accumulation rate on pore close-off in layered firn, The Cryosphere, 8, 91–105, doi:10.5194/tc-8-91-2014, 2014. 5649

Griggs, J. and Bamber, J.: Antarctic ice-shelf thickness from satellite radar altimetry, J. Glaciol., 57, 485–498, doi:10.3189/002214311796905659, 2011. 5649

TCD
9, 5647–5680, 2015

Hempel, L., Thyssen, F., Gundestrup, N., Clausen, H. B., and Miller, H.: A comparison of radio-echo sounding data and electrical conductivity of the GRIP ice core, J. Glaciol., 46, 369–374, doi:10.3189/172756500781833070, 2000. 5650

Herron, M. M. and Langway, C. C.: Firn densification: an empirical model, J. Glaciol., 25, 373–385, 1980. 5649

Hörhold, M. W., Kipfstuhl, S., Wilhelms, F., Freitag, J., and Frenzel, A.: The densification of layered polar firn, J. Geophys. Res., 116, F01001, doi:10.1029/2009JF001630, 2011. 5649

Hörhold, M. W., Laepple, T., Freitag, J., Bigler, M., Fischer, H., and Kipfstuhl, S.: On the impact of impurities on the densification of polar firn, Earth Planet. Sc. Lett., 325, 93–99, doi:10.1016/j.epsl.2011.12.022, 2012. 5649

Hubbard, B. and Glasser, N.: Field Techniques in Glaciology and Glacial Geomorphology, John Wiley & Sons Ltd., The Atrium, Southern Gate, Chichester, West Sussex, 2005. 5650

Hubbard, B., Roberson, S., Samyn, D., and Merton-Lyn, D.: Digital optical televiewing of ice boreholes, J. Glaciol., 54, 823–830, doi:10.3189/002214308787779988, 2008. 5661

Hubbard, B., Tison, J.-L., Philippe, M., Heene, B., Pattyn, F., Malone, T., and Freitag, J.: Ice shelf density reconstructed from optical televiewer borehole logging, Geophys. Res. Lett., 40, 5882–5887, doi:10.1002/2013GL058023, 2013. 5649, 5653, 5660, 5661

Kawamura, T.: Nondestructive, three-dimensional density measurements of ice core samples by X ray computed tomography, J. Geophys. Res.-Sol. Ea., 95, 12407–12412, doi:10.1029/JB095iB08p12407, 1990. 5649

Kovacs, A., Gow, A. J., and Morey, R. M.: The in-situ dielectric constant of polar firn revisited, Cold Reg. Sci. Technol., 23, 245–256, doi:10.1016/0165-232X(94)00016-Q, 1995. 5650

Langley, K., von Deschwanden, A., Kohler, J., Sinisalo, A., Matsuoka, K., Hattermann, T., Humbert, A., Nøst, O. A., and Isaksson, E.: Complex network of channels beneath an Antarctic ice shelf, Geophys. Res. Lett., 41, 1209–1215, doi:10.1002/2013GL058947, 2014. 5650

Le Brocq, A., Ross, N., Griggs, J., Bingham, R., Corr, H., Ferraccioli, F., Jenkins, A., Jordan, T., Payne, A., Rippin, D., and Siegert, M.: Evidence from ice shelves for channelized meltwater flow beneath the Antarctic Ice Sheet, Nat. Geosci., 6, 945–948, doi:10.1038/ngeo1977, 2013. 5650

Lenaerts, J. T. M., Brown, J., van den Broeke, M. R., Matsuoka, K., Drews, R., Callens, D., Philippe, M., Gorodetskaya, I. V., van Meijgaard, E., Reijmer, C. H., Pattyn, F., and van Lipzig, N. P. M.: High variability of climate and surface mass balance induced by Antarctic ice rises, J. Glaciol., 60, 1101–1110, doi:10.3189/2014JoG14J040, 2014. 5651

TCD
9, 5647–5680, 2015

Ligtenberg, S. R. M., Kuipers Munneke, P., and van den Broeke, M. R.: Present and future variations in Antarctic firn air content, The Cryosphere, 8, 1711–1723, doi:10.5194/tc-8-1711-2014, 2014. 5649, 5658, 5666

Looyenga, H.: Dielectric constants of heterogeneous mixtures, Physica, 31, 401–406, 1965. 5650

Margrave, G. F.: Numerical Methods of Exploration Seismology with algorithms in Matlab, CREWES Toolbox Version: 1006, CREWES Department of Geoscience, University of Calgary, Calgary, 2011. 5656

Matsuoka, K., Wilen, L., Hurley, S. P., and Raymond, C. F.: Effects of birefringence within ice sheets on obliquely propagating radio waves, IEEE T. Geosci. Remote, 47, 1429–1443, doi:10.1109/TGRS.2008.2005201, 2009. 5665

Matsuoka, K., Pattyn, F., Callens, D., and Conway, H.: Radar characterization of the basal interface across the grounding zone of an ice-rise promontory in East Antarctica, Ann. Glaciol., 53, 29–34, doi:10.3189/2012AoG60A106, 2012a. 5652

Matsuoka, K., Power, D., Fujita, S., and Raymond, C. F.: Rapid development of anisotropic ice-crystal-alignment fabrics inferred from englacial radar polarimetry, central West Antarctica, J. Geophys. Res.-Earth, 117, F03029, doi:10.1029/2012JF002440, 2012b. 5665

Murray, T., Stuart, G. W., Miller, P. J., Woodward, J., Smith, A. M., Porter, P. R., and Jiskoot, H.: Glacier surge propagation by thermal evolution at the bed, J. Geophys. Res.-Sol. Ea., 105, 13491–13507, doi:10.1029/2000JB900066, 2000. 5650

Rignot, E., Jacobs, S., Mouginot, J., and Scheuchl, B.: Ice-Shelf Melting Around Antarctica, Science, 341, 266–270, doi:10.1126/science.1235798, 2013. 5649

Sergienko, O. V.: Basal channels on ice shelves, J. Geophys. Res.-Earth, 118, 1342–1355, doi:10.1002/jgrf.20105, 2013. 5650

Stanton, T. P., Shaw, W. J., Truffer, M., Corr, H. F. J., Peters, L. E., Riverman, K. L., Bindschadler, R., Holland, D. M., and Anandakrishnan, S.: Channelized ice melting in the ocean boundary layer beneath Pine Island Glacier, Antarctica, Science, 341, 1236–1239, doi:10.1126/science.1239373, 2013. 5650

van den Broeke, M., van den Berg, W. J., and van den Meijgaard, E.: Firn depth correction along the Antarctic grounding line, Antarct. Sci., 20, 513–517, doi:10.1017/S095410200800148X, 2008. 5665

TCD
9, 5647–5680, 2015

Waddington, E. D., Neumann, T. A., Koutnik, M. R., Marshall, H.-P., and Morse, D. L.: Inference of accumulation-rate patterns from deep layers in glaciers and ice sheets, J. Glaciol., 53, 694–712, doi:10.3189/002214307784409351, 2007. 5649

Wharton, R. B., Rau, R., and Best, D. L.: Electromagnetic propagation logging: advances in technique and interpretation, paper presented at the SPE Annual Technical Conference and Exhibition, 21–24 September, Dallas, Texas, doi:10.2118/9267-MS, 1980. 5650, 5654

Wilhelms, F., Kipfstuhl, S., Miller, H., Heinloth, K., and Firestone, J.: Precise dielectric profiling of ice cores: A new device with improved guarding and its theory, J. Glaciol., 44, 171–174, 1998. 5649

Winebrenner, D. P., Smith, B. E., Catania, G. A., Conway, H. B., and Raymond, C. F.: Radio-frequency attenuation beneath Siple Dome, West Antarctica, from wide-angle and profiling radar observations, Ann. Glaciol., 37, 226–232, doi:10.3189/172756403781815483, 2003. 5650, 5665

Wouters, B., Martin-Español, A., Helm, V., Flament, T., van Wessem, J. M., Ligtenberg, S. R. M., van den Broeke, M. R., and Bamber, J. L.: Dynamic thinning of glaciers on the Southern Antarctic Peninsula, Science, 348, 899–903, doi:10.1126/science.aaa5727, 2015. 5649

Yilmaz, O.: Seismic Data Processing, Society of Exploration Geophysicists, Tulsa, OK, 1987. 5651, 5664

Zelt, C. A. and Smith, R. B.: Seismic traveltime inversion for 2-D crustal velocity structure, Geophys. J. Int., 108, 16–34, doi:10.1111/j.1365-246X.1992.tb00836.x, 1992. 5650, 5651, 5656

Zwally, H. J. and Jun, L.: Seasonal and interannual variations of firn densification and ice-sheet surface elevation at the Greenland summit, J. Glaciol., 48, 199–207, doi:10.3189/172756502781831403, 2002. 5649

TCD
9, 5647–5680, 2015

Table 1. Summary of the WARR results from site 1–5 in terms of range of offsets, number of offsets (O), ice thickness (H), depth-averaged density ($\overline{\rho}$), depth-averaged radio-wave propagation speed ($\overline{v}$), firn-air content (H_A), and the decay length (r) parameterizing the depth–density function. The ranges correspond to the lower and upper limit of five reflector combination at each site (four reflector combinations contain three reflectors, and one combination all four reflectors).

#	offset range (m)	O	H (m)	$\overline{\rho}$ (kg m^{-3})	$\overline{v}$ (m µs^{-1})	H_A (m)	r (m^{-1})
1	26–308	141	280.2–281.3	847–855	173.0–173.8	16.8–19.3	0.026–0.030
2	30–318	144	266.1–266.6	864–867	171.9–172.2	12.4–13.2	0.039–0.041
3	20–222	101	156.7–157.0	828–832	175.2–175.5	13.3–14.0	0.036–0.038
4	25–366	170	292.9–293.4	850–859	172.6–173.4	16.1–19.0	0.027–0.032
5	20–404	142	395.0–396.1	872–874	171.2–171.5	15.2–16.4	0.031–0.036

TCD
9, 5647–5680, 2015

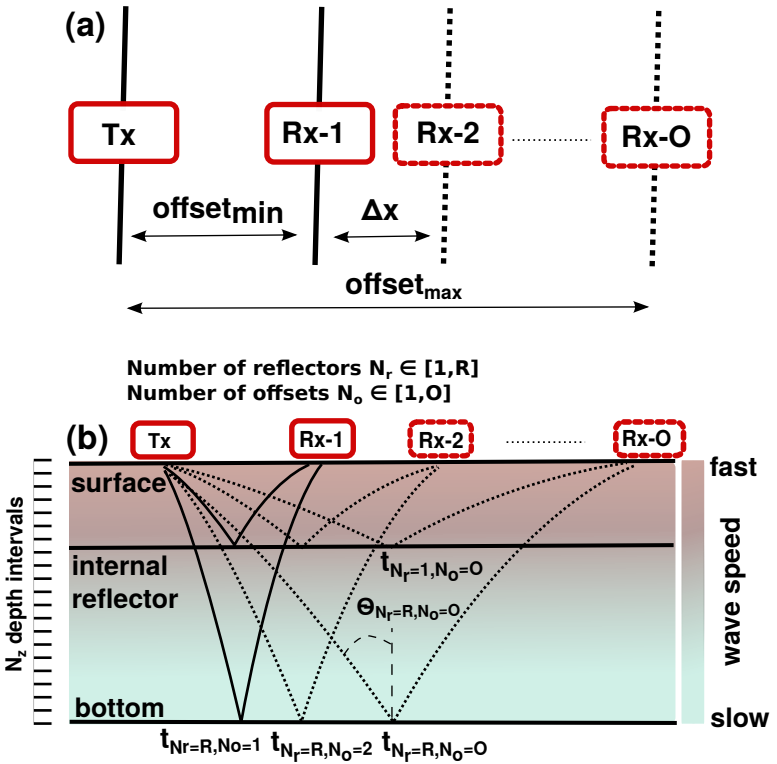

Figure 1. (a) Plain view of the wide-angle acquisition geometry: Transmitting (Tx) and receiving (Rx) antennas were aligned in parallel. While the transmitter remained at a fixed location, the receiver was incrementally moved farther away. A sketch of the corresponding raypaths is shown in **(b)** with a synthetic velocity–depth function color coded. The labels of example rays and their incidence angles are presented in Eqs. (1)–(10).

TCD
9, 5647–5680, 2015

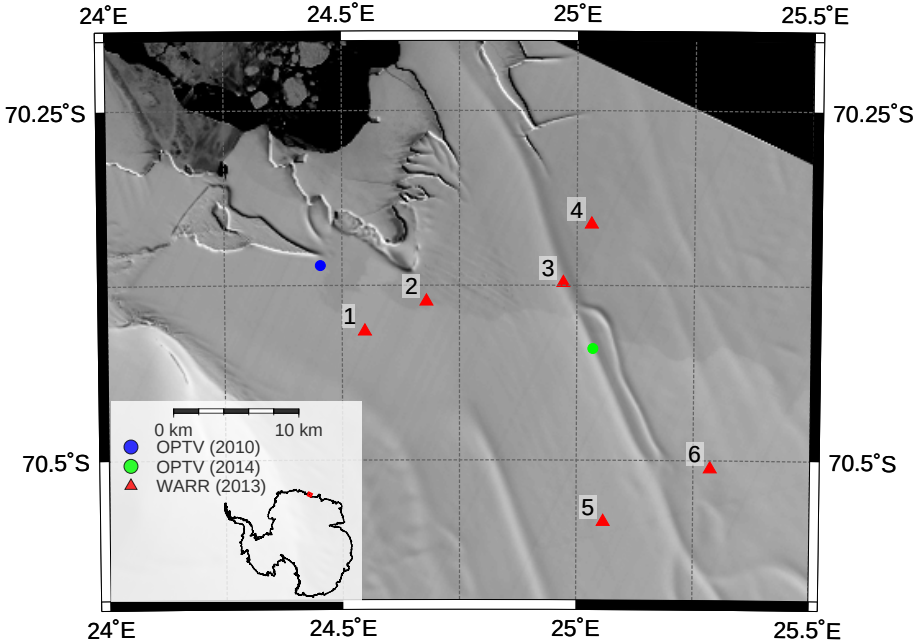

Figure 2. Location of the wide-angle (WARR) radar sites (red triangles) relative to the boreholes of 2010 and 2014 which were used for optical televiewing (OPTV). The depressed surfaces of ice-shelf channels appear as elongated lineations in the background image (Landsat 8, December 2013 provided by the US Geological Survey).

TCD
9, 5647–5680, 2015

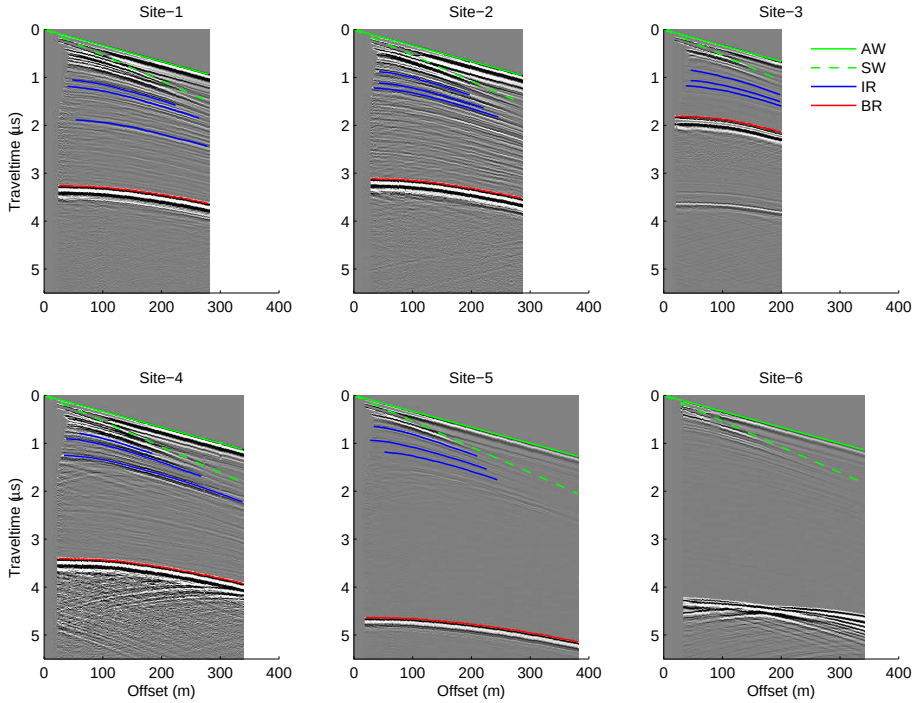

Figure 3. Wide-angle radar data showing air waves (AW, green lines) and surface waves (SW, green dashed lines) with linearly increasing traveltime with offset, while traveltime increases hyperbolically with offset for internal (blue) and basal (red) reflectors. See Fig. 2 for locations of Sites 1–6. Site 6 was excluded from further analysis because the basal reflection is ambiguous (probably due to off-angle reflectors in the vicinity).

TCD
9, 5647–5680, 2015

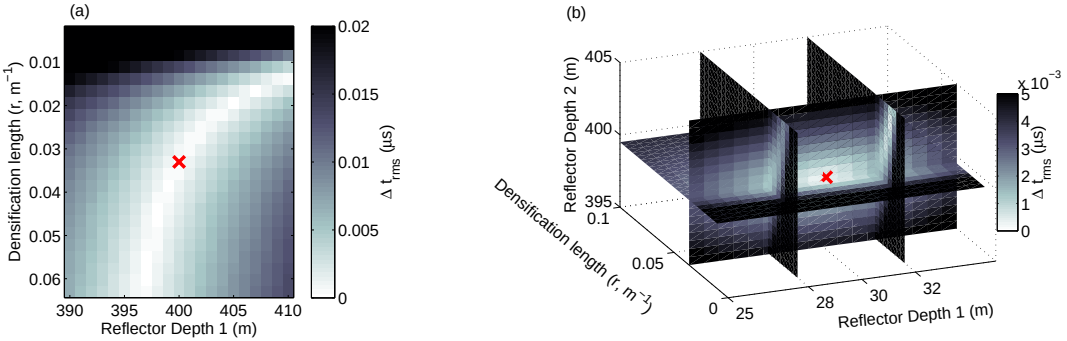

Figure 4. Traveltime residuals (Δt_{rms}) calculated with raytracing between ideal reflector in a fixed depth–density profile ($A = 460\,\mathrm{kg\,m^{-3}}$; $r = 0.033\,\mathrm{m^{-1}}$) with reflectors perturbed in terms of depths and density. Ideal solutions are marked with red crosses: **(a)** traveltime residuals for an ideal reflector at 400 m depth; **(b)** volumetric slice plot of traveltime residuals for two idealised reflectors at 30 and 400 m depth.

TCD
9, 5647–5680, 2015

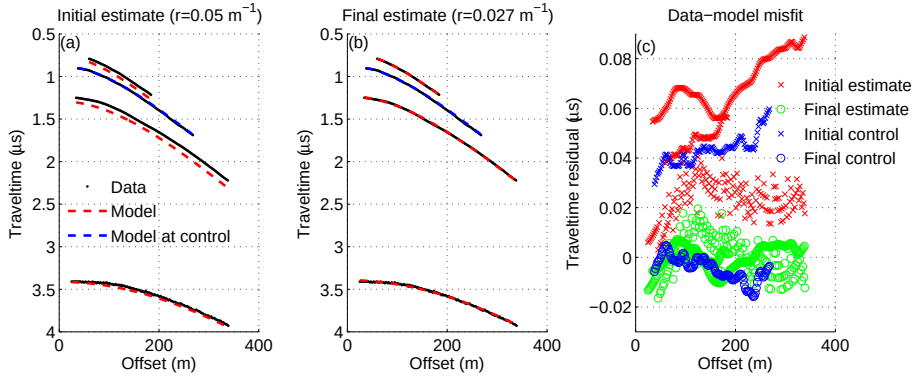

Figure 5. Example for initial **(a)** and final **(b)** fit between the raytracing forward model and the reflectors at Site 2. In this case, three reflectors (black dots) were used for the inversion and one reflector was kept for control. The forward model corresponds to the red dashed curves and the control reflectors to the blue dashed curves. Initial estimates shown here were $r^0 = 0.05\,\mathrm{m}^{-1}$, $D_1 = 68.2\,\mathrm{m}$, $D_3 = 112.9\,\mathrm{m}$, $D_4 = 291.2\,\mathrm{m}$; the best fit resulted in $r = 0.027\,\mathrm{m}^{-1}$, $D_1 = 67.7\,\mathrm{m}$, $D_3 = 111.2\,\mathrm{m}$, and $D_4 = 293.3\,\mathrm{m}$. The traveltime residual between model and data for initial (x) and final fit (o) are shown in **(c)**.

TCD
9, 5647–5680, 2015

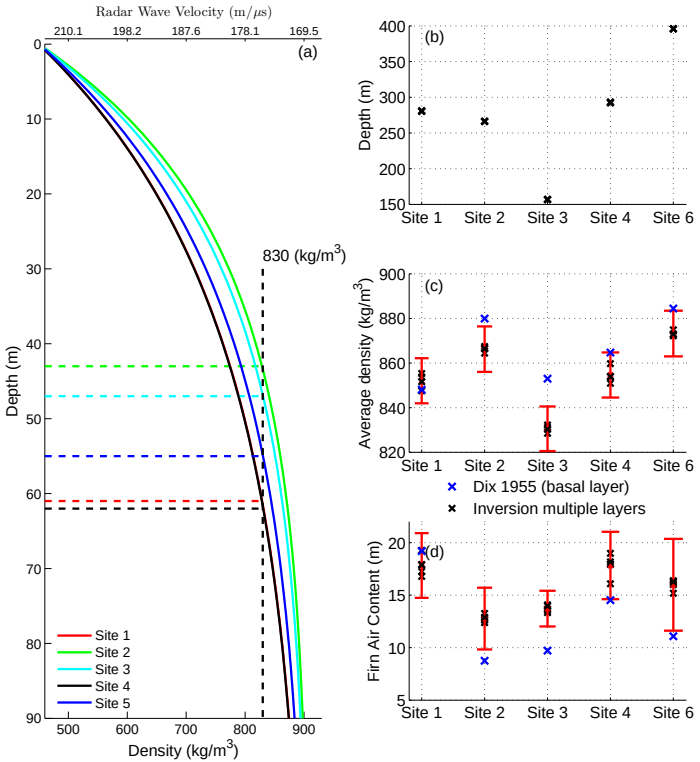

Figure 6. Derived data summary of all sites (Site 3 is located in an ice-shelf channel): **(a)** depth–density profiles inverted from four reflectors, **(b)** ice thickness, **(c)** depth-averaged density, and **(d)** firn-air content. Black crosses in **(b)**–**(d)** represent the outcomes for five combinations containing three or more reflectors. Error bars assume a 1 % error in depth-averaged radio-wave propagation speed. The blue crosses correspond to depth-averaged solutions using normal moveout of the basal reflector only (Dix, 1955).

TCD
9, 5647–5680, 2015

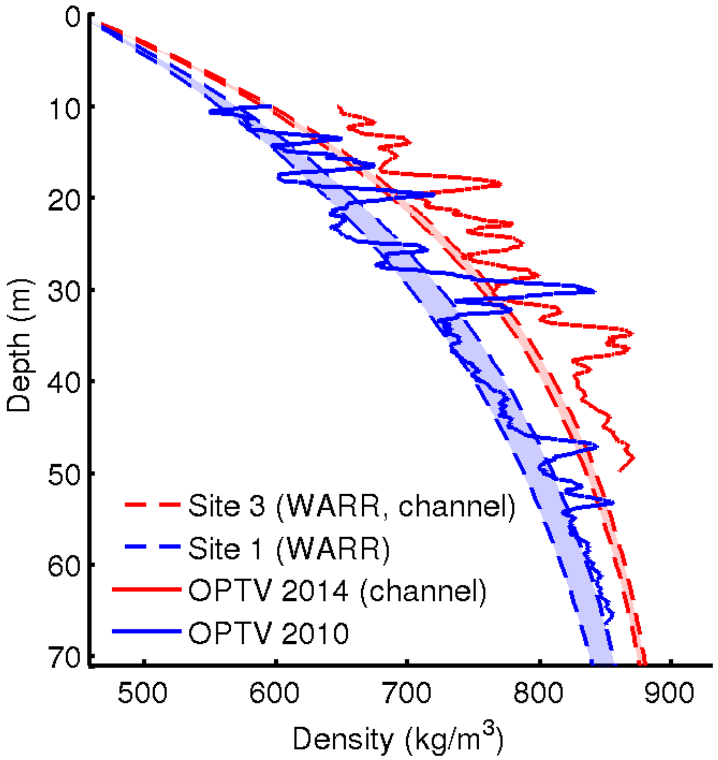

Figure 7. Depth profiles of density derived from WARR (dashed) and OPTV (solid). WARR data are from Sites 1 and 3, closest to the OPTV sites. Site 3 and the 2014 borehole are both in the trough of an ice-shelf channel (Fig. 2). The envelopes of the radar-derived densities correspond to the lower and upper limit of five reflector combinations used for the inversion. The OPTV logs were smoothed with a 0.5 m running mean.

TCD
9, 5647–5680, 2015